






Article

Corrosion Behavior of AA2055 Aluminum-Lithium Alloys Anodized in the Presence of Sulfuric Acid Solution

Pedro Oliver Samaniego-Gómez¹, Facundo Almeraya-Calderon^{1,*}, Erick Maldonado-Bandala², Jose Cabral-Miramontes¹, Demetrio Nieves-Mendoza², Javier Olguin-Coca³, Luis Daimir Lopez-Leon⁴, Luis G. Silva Vidaurri⁴, Patricia Zambrano-Robledo¹ and Citlalli Gaona-Tiburcio^{1,*}

¹ Universidad Autónoma de Nuevo León, FIME-Centro de Investigación e Innovación en Ingeniería Aeronáutica (CIIIA), Av. Universidad s/n, Ciudad Universitaria, San Nicolás de los Garza N.L. 66455, Mexico; pedro.samaniegom@uanl.edu.mx (P.O.S.-G.); jose.cabralmr@uanl.edu.mx (J.C.-M.); patricia.zambranor@uanl.edu.mx (P.Z.-R.)

² Universidad Veracruzana, Facultad de Ingeniería Civil, Xalapa 91000, Mexico; erimaldonado@uv.mx (E.M.-B.); dneives@uv.mx (D.N.-M.)

³ Universidad Autónoma del Estado de Hidalgo, Área Académica de Ingeniería y Arquitectura, Carretera Pachuca-Tulancingo Km. 4.5, Pachuca de Soto 42082, Mexico; olguinc@uaeh.edu.mx

⁴ Centro de Investigación en Materiales Avanzados Subsede Monterrey (CIMAV), Alianza Norte 202, PIIT, Autopista Monterrey-Aeropuerto, Km. 10, Apodaca 66628, Mexico; luis_lopez@uaeh.edu.mx (L.D.L.-L.); luis.silva@cimav.edu.mx (L.G.S.V.)

* Correspondence: facundo.almerayacl@uanl.edu.mx (F.A.-C.); citlalli.gaonatbr@uanl.edu.mx (C.G.-T.)



Citation: Samaniego-Gómez, P.O.; Almeraya-Calderon, F.; Maldonado-Bandala, E.; Cabral-Miramontes, J.; Nieves-Mendoza, D.; Olguin-Coca, J.; Lopez-Leon, L.D.; Silva Vidaurri, L.G.; Zambrano-Robledo, P.; Gaona-Tiburcio, C. Corrosion Behavior of AA2055 Aluminum-Lithium Alloys Anodized in the Presence of Sulfuric Acid Solution. *Coatings* **2021**, *11*, 1278. <https://doi.org/10.3390/coatings11111278>

Academic Editor: Alina Pruna

Received: 15 September 2021

Accepted: 18 October 2021

Published: 21 October 2021

Publisher's Note: MDPI stays neutral with regard to jurisdictional claims in published maps and institutional affiliations.



Copyright: © 2021 by the authors. Licensee MDPI, Basel, Switzerland. This article is an open access article distributed under the terms and conditions of the Creative Commons Attribution (CC BY) license (<https://creativecommons.org/licenses/by/4.0/>).

Abstract: The aim of this work was to evaluate the corrosion behavior of the AA2055 Aluminum-lithium alloy anodized in a sulfuric acid (H₂SO₄) bath, varying the current density of 0.19 and 1 A·cm⁻² and why the sealing solution was water (H₂O) and sodium dichromate (Na₂Cr₂O₇). Anodized samples were exposed to a 10 vol.% H₂SO₄ solution and the electrochemical technique used was electrochemical impedance spectroscopy. Scanning electron microscopy and X-ray photoelectron spectroscopy were employed to characterization of the anodizing layer, determinate morphology and thickness of coatings. The Na₂Cr₂O₇ sealing solution tends to increase the charge transfer resistance and produces a more homogeneous and compact passive oxide layer, and imparts a corrosion inhibition protection to the AA2055. SEM observations indicated that the morphology and thickness of the anodic films formed on AA2055 aluminum-lithium alloy anodized have the best results for both current densities.

Keywords: anodizing; aluminum-lithium 2055 alloy; corrosion; SEM; XPS; electrochemical impedance spectroscopy

1. Introduction

Anodizing is an electrochemical process used to increase the thickness of the oxide layer on the surface of aluminum and its alloys. Anodizing treatment is a method of conversion coatings in an electrolytic cell for surface protection on aluminum and its alloys in aerospace and aeronautical applications [1–6].

The development of the aluminum-lithium alloys (known as the third generation) has been used by the aeronautical and other applications due to its good properties, replacing conventional Al-Cu and Al-Zn alloys, resulting in an increase in payload and fuel efficiency [7,8]. Al-Li alloys have a characteristic that a reduction in density is to their advantage, and lithium, being the lightest metal, would have the greatest influence on reducing the density of aluminum. Another advantage of this alloy is that it has a lower flat mechanical anisotropy, good resistance to SCC and fracture toughness [9–16]. Therefore, low density, high strength and rigidity are one of the main alloys in aircraft manufacturing; for example, reinforcing the fuselage, floor beams and wing stringers

of aircrafts [17]. Over the last decade, it has been reported [16,18–21] that several third-generation alloys have been qualified for use in aircraft such as the Airbus 380; among these alloys is AA2055 (developed by Alcoa), which combines density, mechanical resistance and corrosion properties; density (2.71 g/cm^3) is 4 to 5% less than high-strength 7xxx alloys, mechanical strength is similar to a AA7051 and superior to AA7075 and AA7050 alloys. Corrosion resistance (pitting and SCC) in accelerated environments of the AA2055 alloy is similar to or better than AA7xxx alloys with different heat treatments.

The interaction of aluminum in contact with different atmospheres results in the formation of a protective oxide layer on the surface of aluminum alloys. Localized corrosion and the formation of galvanic microcells in the microstructure can be present in aluminum alloys exposure in corrosive substances, making them susceptible to electrochemical degradation [6,19,22]. With electrochemical treatment of anodizing, it is possible to increase the resistance to corrosion, and improve its mechanical properties by generating a thicker artificial oxide film [19]. Ma et al. mentioned that the aerospace aluminum alloys need surface finishing by anodizing to provide the required corrosion resistance under service conditions [7].

The aluminum anodizing process is generally done with sulfuric acid, which generates a dense oxide layer and has high porosity, good adsorption, thick film layers, and good wear resistance that provides protection against corrosion [5,23]. It can also be combined with organic acids, to achieve improvements on surface adhesion, thickness, and corrosion inhibition, among others [3,5,8,23–25]. In anodizing treatment, the Al_2O_3 layer is formed that is fine, compact, porous, and an external barrier. Being a porous oxide layer, such pores are migration routes for corrosive media, so a sealing stage is necessary to stabilize the Al_2O_3 layer, decrease pore size pores, and increase resistance to corrosion. There are different ways to perform the sealing treatment, which can be carried out through different solutions [22,23]. The best results of the sealing stage depend on the surface chemical reactivity of the porous oxide structure in the samples anodized [5,19–21]. One of the most widely known sealing stages is sodium dichromate ($\text{Na}_2\text{Cr}_2\text{O}_7$); it not only blocks the pores, but also provides inhibition [5,25–28].

The aim of this work was to evaluate the corrosion behavior of the AA2055 Aluminum-lithium alloy anodized with sulfuric acid (H_2SO_4), varying the current conditions 0.19 and $1 \text{ A}\cdot\text{cm}^{-2}$ and H_2O and $\text{Na}_2\text{Cr}_2\text{O}_7$ sealing solution. Electrochemical behavior was studied by electrochemical impedance spectroscopy (EIS) technique, and characterization of the oxide layer of aluminum was done using scanning electron microscopy (SEM) and X-ray photoelectron spectroscopy (XPS). Aluminum alloys in aircraft are exposed to different atmospheres such as marine and industrial (acid rain). Exposure to sulfuric acid can simulate an acid rain environment, which is formed from the chemical reactions of sulfur dioxide and nitrogen oxides found in the atmosphere with water and chemical contaminants that result in nitric and sulfuric acids [29].

2. Materials and Methods

2.1. Metallographic Preparation of Samples

The material used in this study was AA2055, which represents the third generation of the aluminum-lithium alloy. The nominal chemical composition of the AA2055 alloys is shown in Table 1.

Table 1. The nominal chemical composition of AA2055 alloy (wt.%).

Alloy	Elements									
	Cu	Li	Zn	Ag	Mg	Mn	Zr	Fe	Si	Al
2055	3.2–4.2	1.0–1.3	0.30–0.70	0.20–0.70	0.20–0.60	0.10–0.50	0.05–0.15	0.1 max	0.07 max	Balance

The aluminum samples were mechanically polished using metallographic techniques according to ASTM E3 [30]. The material was sequentially polished using different SiC grit

papers with 400, 600, and 800 grades, followed by ultrasonic cleaning in ethanol (C₂H₅OH) and deionized water.

2.2. Anodizing Treatment

The anodizing treatment consisted of the following stages [31]:

- Pretreatment:
 - Degreased and Pickling in a 50 wt.% HCl solution (analytical grade reagents (J.T. Baker, Nuevo León, México) for 5 s at 25 °C
 - Rinsed in distilled water
- Anodizing treatment:
 - Bath = 16 wt.% H₂SO₄ solution (analytical grade reagents (J.T. Baker))
 - Current densities = 0.19 and 1.0 A·cm⁻²
 - Electrolyte pH = 6.0
 - Time = 45 min
 - Temperature = 25 °C
- Sealing treatment:
 - The anodized specimens were immersed in H₂O or in 6 wt.% Na₂Cr₂O₇ solution (analytical grade reagents (J.T. Baker)) at 95 °C for 25 min.

Table 2 shows the nomenclature of different samples (S).

Table 2. Nomenclature and anodizing conditions of different samples.

Alloy	Nomenclature	Sealing Treatment			Anodizing Current Density (A·cm ²)
		Temperature (°C)	Time (min)	Solution	
AA2055	S1	–	–	–	0.19
	S2	95	–	H ₂ O	1.00
	S3	–	25	–	0.19
	S4	–	–	6 wt.% Na ₂ Cr ₂ O ₇	1.00

2.3. SEM Characterization

Microstructural analysis of the surface and in cross sections was done using scanning electron microscope (SEM, JEOL-JSM-5610LV, Tokyo, Japan), operating at 20 KV and a work distance of 12 mm. The surface micrographs by SEM was done using a secondary electrons (SE) detector. Observations of micrographs of the oxide layer thickness in cross sections were done using a backscattered electrons (BSE) detector.

2.4. Electrochemical Impedance Spectroscopy

EIS measurements were conducted at room temperature using an electrochemical Interface mod. 1287A and Impedance Analyzer mod. 1260 Solartron (Bognor Regis, UK) in 10 vol.% H₂SO₄ solution [32–34].

EIS measurements parameters were used in the frequency range from 100 kHz to 1 mHz, with an amplitude of 10 mV sinewave [35,36]. The impedance data were collected and modelled using ZPlot and ZView software (Zview 2.0 software), respectively (Scribner Associates, Southern Pines, NC, USA). Corrosion tests were conducted in triplicate.

2.5. XPS Characterization

XPS analyses were performed to determine the chemical composition of the aluminum oxide layer and were done using the Thermo Fisher Scientific ESCALAB 250 Xi equipment (Waltham, MA, USA) at a pressure of approximately 10 mBar; the excitation of the analyzed photoelectrons was carried out with a monochromatic Al KAlpha X-ray source (1486 eV), analysis radius of μm, as well as the analysis conditions for the high-resolution zones (eV step energy, 45° of “take-off angle” with 0.1 eV step).

3. Results and Discussion

3.1. SEM Microstructural Analysis

The SEM-analyzed micrographs of the oxide layer of AA2055 alloy anodized is of great importance for the corrosion behavior.

Figure 1 shows the surface micrographs by SEM using a secondary electrons (SE) detector for the AA2055 anodized samples (S1, S2, S3, and S4) at different current densities (0.19 and $1 \text{ A}\cdot\text{cm}^{-2}$) and sealing in H_2O and $\text{Na}_2\text{Cr}_2\text{O}_7$ solutions. Figure 1a shows a heterogeneous surface compared to the superficial micrographs of Figure 1b–d. In the surface micrographs of sample S1, there are areas with a series of bumps and some bright precipitations derived from substrate elements and impurities. Herrera et al. [37] mentioned that these impurities affect the homogeneity of the passive layer and are present because they were not completely removed during mechanical polishing or in the stage prior to anodizing. Some authors [17,38,39] have reported that the micrometric scale defects present on the surface of the anodic film have had a similar behavior in the AA2099 alloy due to the high copper content. Figure 1c,d shows samples S3 and S4 with some imperfections (cavity) on the surface; this may be due to varying the current density, the sealing solutions and the preferential dissolution of intermetallic phases, during the growth of the Al_2O_3 layer in the H_2SO_4 bath, resulting in a no-uniform surface [40].

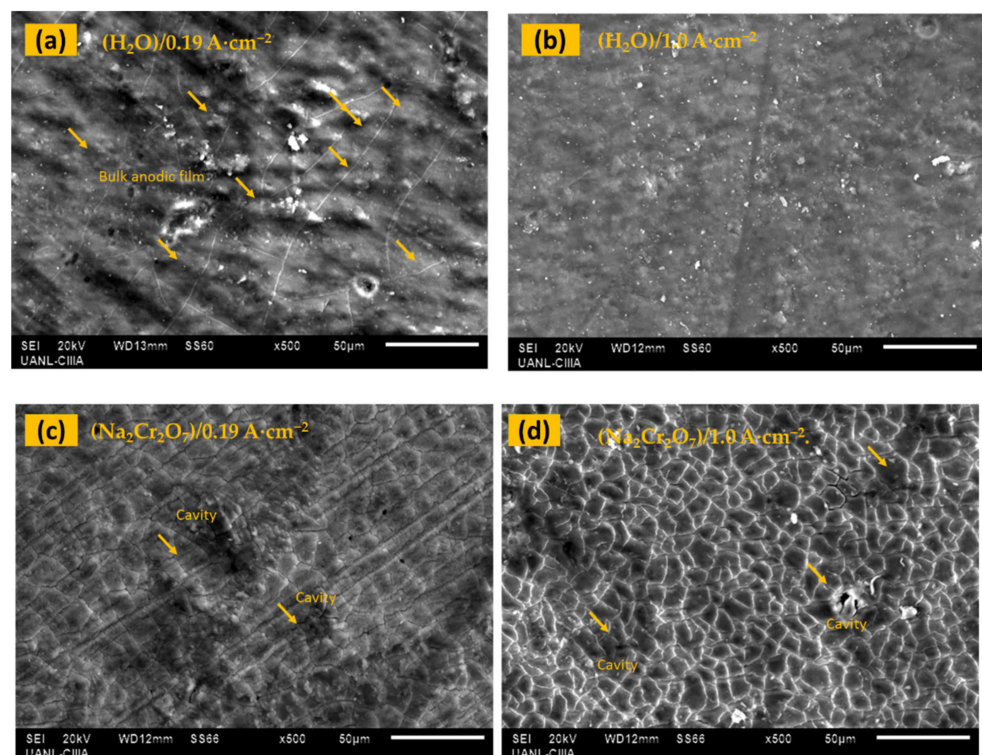


Figure 1. SEM-SEI surface micrographs of the anodized AA2055 alloys with different sealing treatments: (a) S1, (b) S2, (c) S3, and (d) S4.

Figure 2 shows the micrographs obtained by scanning electron microscope using a backscattered electrons (BSE) detector for cross section anodized samples and their average thickness of the anodic oxide film. The current density of 0.19 and $1 \text{ A}\cdot\text{cm}^{-2}$ did not influence the oxide film; homogeneity is observed in all samples. The average thickness in the anodized samples is between 4.33 and $5.41 \mu\text{m}$. The thickness of the aluminum oxide layer of coating greatly depends on the current density, the bath, and the time of anodization [41].

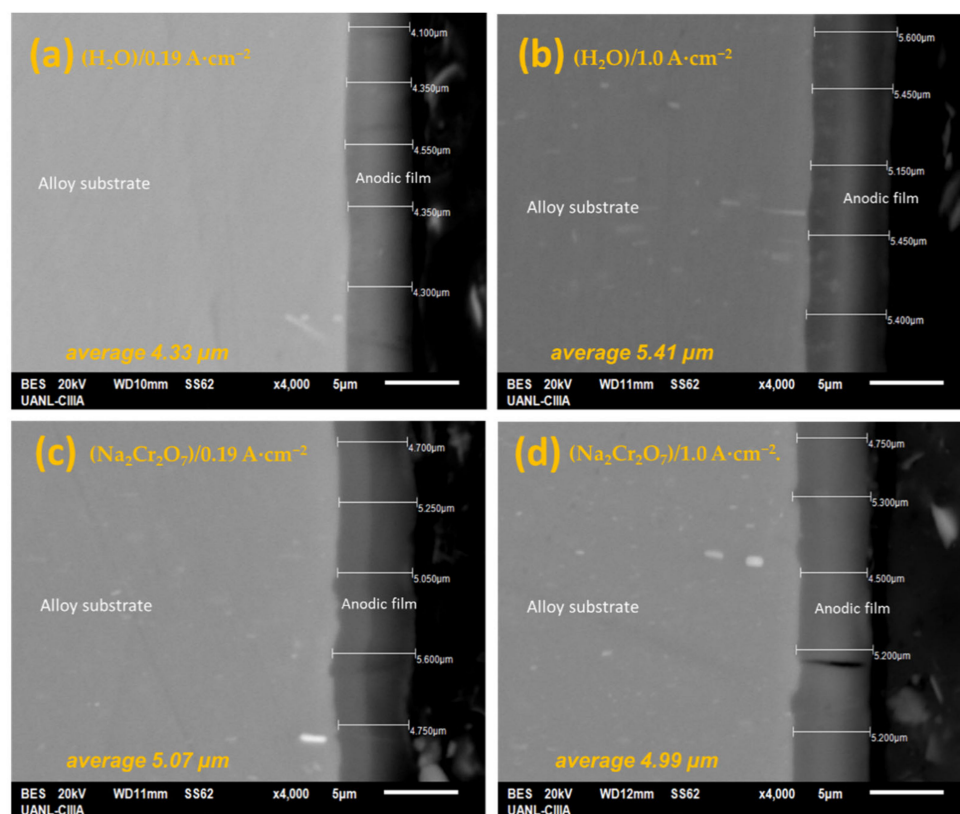


Figure 2. SEM-BES cross-sectional micrographs of the anodized AA2055 samples with different sealing treatments: (a) S1, (b) S2, (c) S3, and (d) S4.

3.2. Electrochemical Impedance Spectroscopy Analysis

Figure 3 shows Nyquist diagrams, for anodized and sealed Al-Li AA2055 alloy immersed in 10 vol.% H_2SO_4 solution. In all samples, a capacitive loop is observed at high frequencies, at intermedium frequencies, it observed a capacitive behavior, and finally, in low frequency, we see an inductive loop having origin at frequencies between 0.20 and 0.01 Hz, which is presented in the fourth quadrant. The two capacitive loops associated at high and intermediate frequencies can be related to the ingress of the corrosive medium through the surface of the anodic coating. This is due to the surface defects seen in Figures 1 and 2, which in some cases extend to the surface of the metallic substrate. For the inductive loop observed at low frequencies, some authors have proposed different origins, among which it may be attributed to the disturbance induced by redissolution of the oxide layer formed in the anodizing process, to the species adsorption–desorption processes and related to the existence of a passive current [42–44]. According to Bastidas, Jirón, Jinlong, and Alexe [45–49], the adsorption–desorption processes on the anodized surface origin negative values of capacitance and resistance. Information provided by the diameter of the semicircle corresponding to resistance of the process is occurring [50–55].

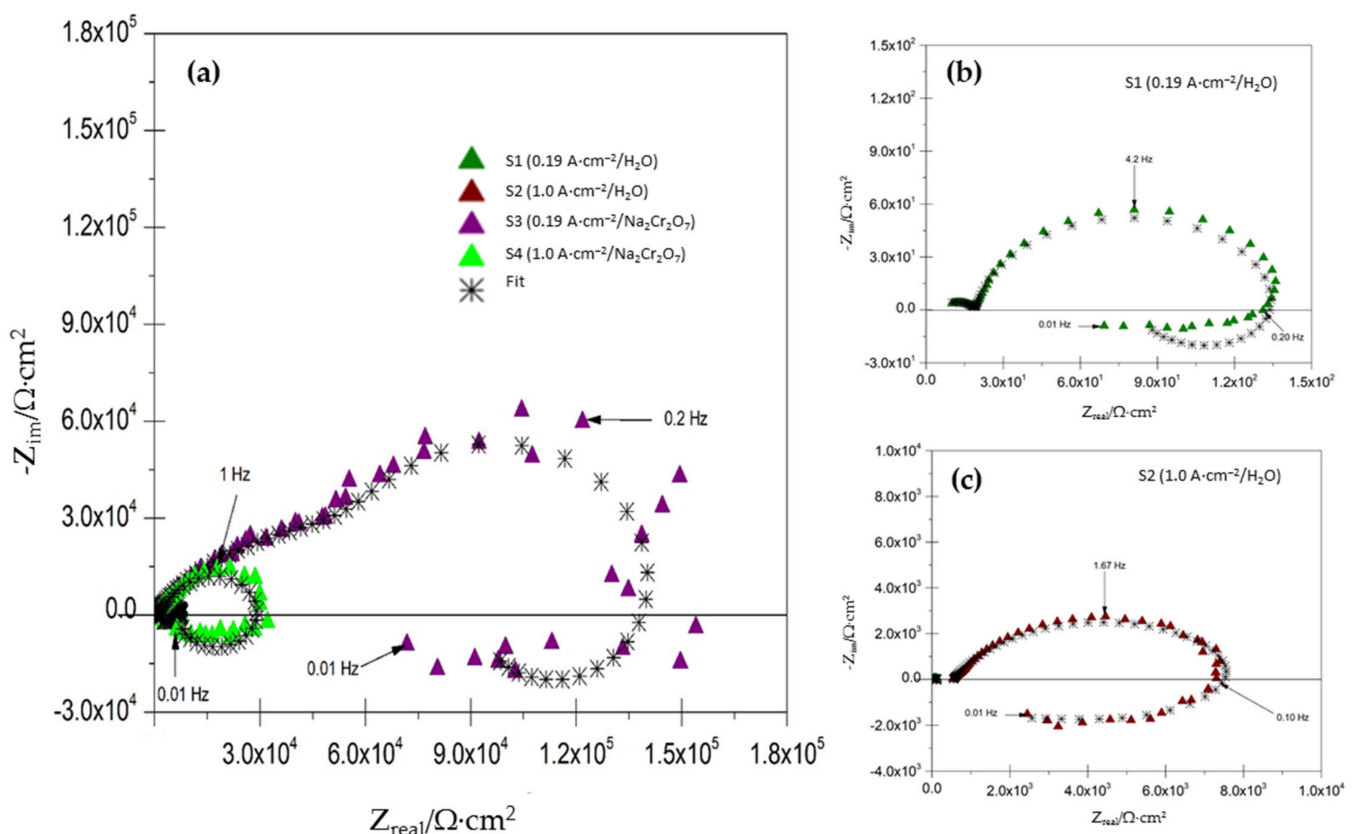


Figure 3. Nyquist diagrams of anodized AA2055 samples immersed to 10 vol.% H_2SO_4 : (a) S1–S4, (b) S1 and (c) S2.

Because of the presence of heterogeneities in barrier and porous layers, their capacitive behavior is better simulated by constant phase elements (CPE) than by a simple capacitance (C) of the electrochemical mechanism by interfacial charge storage. Fitting of the impedance data was accomplished using the equivalent circuit shown in Figure 4. Using this software (Zview 2.0 by Scribner Associates, Southern Pines, NC, USA), all the circuit parameters were adjusted simultaneously in order to fit the measured data and to obtain resistances, capacitances, relaxation frequencies, and the equivalent circuit of the materials under study. The impedance response provided by the equivalent circuit models simulates the experimental data accurately. As a result of the impedance measurements obtained, three-time constants are identified, which were adjusted using the equivalent electrical circuit model (EEC). Using CPE generally, increases in fit [56–59] and in corrosion studies, CPE are more often used to describe the frequency dependence of non-ideal capacitive behavior. Below is a CPE defined as according to the mathematical definition by Equation (1):

$$Z_{\text{CPE}} = \frac{1}{Y(j\omega)^n} \quad (1)$$

where Y = admittance (the reciprocal of electrochemical impedance), $j^n = (-1) =$ imaginary number, ω = angular frequency, and n = dimensionless fraction exponent ($-1 < n < +1$). CPE is an ideal capacitor ($n = +1$) and is an inductor ($n = -1$) [45,54,60–67]. The electrical processes at layers in anodized samples have been related to the EEC model that contains the electrolyte resistance (R_s), resistance due to the sealing effect is a parallel combination ($R1//CPE1$); $R1$ is in series with a second $R2//CPE2$ for resistance of the porous layer; and, finally, resistance ($R3$) and a constant phase element (CPE3) correspond to resistance of the barrier layer.

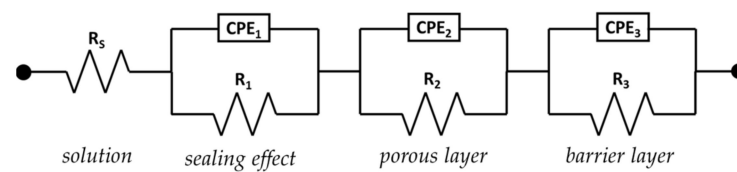


Figure 4. The proposed electrical equivalent circuit (EEC) model.

Table 3 shows the EIS measurements obtained by EEC simulation of AA2055 Aluminum-Lithium alloys anodized and exposed to 10 vol.% H₂SO₄ solutions. In the samples (S1–S4), the χ^2 values are in the interval of 1.48×10^{-2} – 9.49×10^{-3} represented, and the simulations carried out by the proposed equivalent circuit can be used. The variation of resistance solution (R_s) value in the interval of 4.6490–520.9189 $\Omega \cdot \text{cm}^2$ is due in most cases to the morphology of the anodic layer, which is associated with the surface charge and the double electrochemical layer generated between the electrolyte and the surface [68]. Y_1 , Y_2 , and Y_3 stand for sealing effect admittance, porous layer admittance, and barrier layer admittance, respectively in the ECC. The values of the resistance R_1 , which are in an interval of 14.78 to 4121 $\Omega \cdot \text{cm}^2$, correspond to the sealing effect; R_2 have a value of 128 to 208,920 $\Omega \cdot \text{cm}^2$, which represents the resistance of the porous layer, and finally, R_3 with values of -66.77 to $-67,814 \Omega \cdot \text{cm}^2$ is the resistance of the barrier layer. The resistance to charge transfer (R_{ct}) is the sum of the absolute value of the resistances R_1 , R_2 , and R_3 , which can be directly related to the corrosion resistance of the anodic layers formed during the anodizing process and sealing solution. In samples S3 and S4, the high resistance values (R_1 , R_2 , and R_3) were presented, which indicates that sealing in Na₂Cr₂O₇ solution produces anodic layers more resistant to corrosion. This behavior is related in some articles to the formation of compounds between the aluminum oxide and the chromium present in the sealing solution, benefiting the corrosion resistance properties of the film formed. Compounds formed in the sodium dichromate sealing process can be aluminum oxydichromate [Al(OH)CrO₄], or aluminum oxychromate [(AlO)₂CrO₄], which are formed in the micropores; additionally the residual hexavalent chromium acts as a corrosion inhibitor [69–71]. The highest values of R_{ct} were present in sample S3 (anodized with 0.19 A·cm⁻² and sealed with Na₂Cr₂O₇ solution) and the lowest values were for sample S2 (H₂O sealing solution), which can be due to the porosity of the aluminum oxide layer, which does not completely reduce the diameter of the pore when it is sealed with water. The n_1 value is medium (0.6290–0.7961), the significance of a homogeneous surface of the anodic oxide layer. The n_2 value is high (0.5585–0.9032), indicating a producing depressed semicircle, which may be attributed to the homogeneity of the porous layer, and the n_3 (0.5390–0.7795) parameter value is medium–high, which may be attributed to the homogeneity of the barrier layer [69–74]. The negative values of R_3 and Y_3 that correspond to the barrier layer can be explained as follows: negative capacitance occurs when the surface layer generated by different species on the surface decreases and the negative resistance is due to the interaction between the adsorption and electrodisolution of the oxide layer; negative resistances can also occur in a passive–active transition of electrochemical systems, and these negative values of capacitance and resistance occur when the systems are unstable [75–79].

Table 3. EIS measurements obtained by EEC simulation of AA2055 aluminum-lithium alloys.

Samples	R_s ($\Omega \cdot \text{cm}^2$)	R_1 ($\Omega \cdot \text{cm}^2$)	Y_1 ($\mu\text{s}^{n_1} \cdot \text{cm}^{-2}$)	n_1	R_2 ($\Omega \cdot \text{cm}^2$)	Y_2 ($\mu\Omega\text{s}^{n_2} \cdot \text{cm}^{-2}$)	n_2	R_3 ($\Omega \cdot \text{cm}^2$)	Y_3 ($\mu\Omega\text{s}^{n_3} \cdot \text{cm}^{-2}$)	n_3	χ^2
S1	4.6490 ± 0.23	14.78 ± 0.73	19.4996 ± 0.97	0.6637	128 ± 6.40	462.4946 ± 23.12	0.9032	-66.77 ± 3.33	-0.000275 ± 1.37 × 10 ⁻⁵	0.7724	9.49 × 10 ⁻³
S2	520.9189 ± 26.04	1459 ± 72.95	22.1623 ± 1.10	0.6725	7680 ± 384	9.7601 ± 0.48	0.7725	-7452 ± 372.6	-319.4101 ± 15.97	0.7795	8.95 × 10 ⁻³
S3	60.9330 ± 3.04	4121 ± 206.05	0.28 07 ± 0.01	0.7961	208,920 ± 10,446	3.2972 ± 0.16	0.5585	-67,814 ± 3390.7	-2.0652 ± 0.10	0.5788	1.65 × 10 ⁻²
S4	20.6851 ± 1.03	1770 ± 88.50	4.1416 ± 0.20	0.6290	47,900 ± 2395	9.8849 ± 0.49	0.6653	-35,940 ± 1797	-0.4468 ± 0.02	0.5390	1.48 × 10 ⁻²

3.3. XPS Surface Analysis

To determine the surface chemical composition of the oxide layer and valence states in the Al-Li AA2055 alloy, anodized the samples were investigated by XPS, as shown in Figures 5 and 6. Spectral analysis was performed using Avantage software of Thermo Fisher Scientific equipment (Waltham, MA, USA). To carry out chemical analysis, it is necessary to make the calculations of the deconvolution or contributions that the experimental spectrum contains, and assignment of the elements or compounds is through the peaks binding energy (they may be simple, doublets/satellites) using the database NIST (National Institute of Standards and Technology; Gaithersburg, MD, USA).

Figures 5 and 6 show high-resolution XPS spectra that were collected for Al 2p and O 1s. X-ray photoelectron spectra for Al 2p are shown in Figure 5a–d. Five chemical species found Al_2O_3 , Al_2S_3 , Al_2SiO_5 , $\text{Al}(\text{OH})_3$, $\text{Al}(\text{OH})$, and Cr_2O_3 . The binding energy range for the high-resolution spectra for Al 2p where this behavior occurs is 73.85 to 76.88 eV; see the table of results of the parameters obtained from the peak binding energy and full width at half maximum (FWHM) fitting in Figure 5a'–d', respectively.

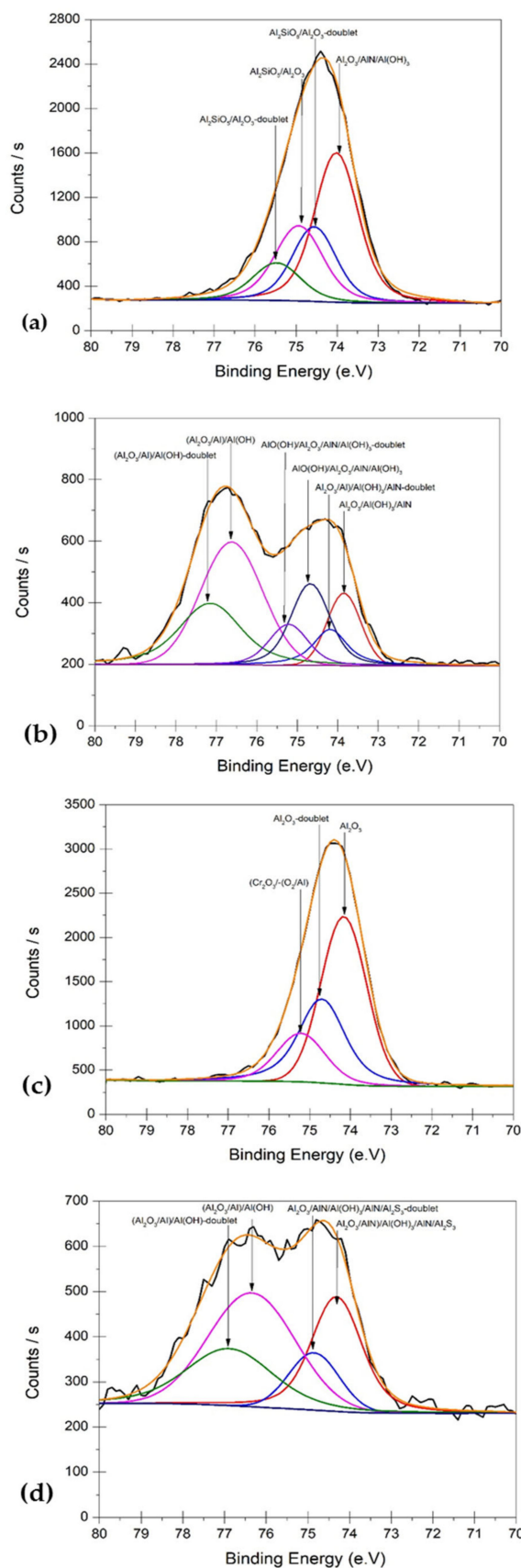
According to some authors, the peak of the binding energy of metallic aluminum is presented at 71.6 eV, which was not detected in the outer layer of the surface of the anodized aluminum of this work. However, the peaks of oxides and aluminum hydroxides (Figure 5) with values approximate of 74.5 eV [80]. For this reason, it can be considered the FWHM with a value of 0.99 in Figure 5b' related to the binding energy of 73.85 and 74.19 eV, corresponding to aluminum oxides and hydroxides, since the separation between the peaks of metallic aluminum and oxides and hydroxides have been reported with binding energy values of 2.5 and 3.7 eV, which depend on the thickness and the growth process of the oxide [81]. In the XPS spectra for Al 2p, a displacement of the binding energy peaks is observed (Figure 5b–d); when there is an increase in the current of the anodizing process influences, the structure of the oxide of the samples under study is independent of the sealing solution [82]. In this investigation, the presence of Cr_2O_3 was detected in the samples sealed with $\text{Na}_2\text{Cr}_2\text{O}_7$, this may be due to a migration process of the chromate ions into the interior of the Al oxide layer shown in Figures 5c and 6c,d. According to the literature [81–85], the non-detection of compound suggests that their concentration has not reached the necessary critical level, probably because they integrate very low solubility second-phase particulates instead of being in solid solution.

The contributions of O 1s can be observed in the XPS spectra, where they reveal the typical binding energies for O 1s, from 530.62 to 532.8 eV according to the Gauss–Lorentz peak (Figure 6a–d). The presence of oxygen in the form of aluminum oxide and hydroxides on the surface could be attributed to the presence of OH[−] and water groups by the sealing solutions, respectively.

The presence of SiO_2 in the XPS spectra of the O 1s orbital, whose binding energy is between 531.28 and 533.59 eV, Figure 6a'–d', can be attributed to different reasons such as: mechanical polishing, impurity in the anodizing bath or the sealing solution. In some works, different species have been found in the oxides produced by the anodizing process from aged baths; however, this difference was not significant in these works [40].

See table results of the parameters obtained, Figure 6a–d [41,76–80].

XPS spectra for Al-Li AA2055 alloy: Figure 5—(a) element Al 2p for S1 sample, (b) Al 2p—S2, (c) Al 2p—S3, (d) Al 2p—S4, and Figure 6—(a) element O 1s—S1 sample, (b) O 1s—S2, (c) O 1s—S3, (d) O 1s—S4, of the chromate ions into the interior of the Al oxide layer [65]. The results of AA2055 specimens sealed H_2O presented a surface film rich Al_2O_3 and $\text{Al}(\text{OH})$; this is attributed to the anodizing and sealing process, while for the $\text{Na}_2\text{Cr}_2\text{O}_7$ sealing, the Al_2O_3 was the main aluminum oxide found on the surface [86–94].



S1 (0.19 A·cm⁻²/H₂O)

Compound	Peak Binding Energy (e.V)	Area Ratio	FWHM fit param (eV)
$Al_2O_3/AlN/Al(OH)_3$	74.02	1	1.26
$Al_2O_3/AlN/Al(OH)_3$ -doublet	74.56	0.5	1.26
Al_2SiO_5/Al_2O_3	74.93	0.55	1.38
Al_2SiO_5/Al_2O_3 -doublet	75.47	0.28	1.38

(a')

S2 (1.0 A·cm⁻²/H₂O)

Compound	Peak Binding Energy (e.V)	Area Ratio	FWHM fit param (eV)
$Al_2O_3/Al(OH)_3/AlN$	73.85	0.32	0.99
$Al_2O_3/Al(OH)_3/AlN$ -doublet	74.19	0.22	0.99
$(Al_2O_3/Al)/Al(OH)$	76.62	1	1.8
$(Al_2O_3/Al)/Al(OH)$ -doublet	77.15	0.59	1.8
$AlO(OH)/Al_2O_3/AlN/Al(OH)_3$	74.68	0.46	1.13
$AlO(OH)/Al_2O_3/AlN/Al(OH)_3$ -doublet	75.22	0.23	1.13

(b')

S3 (0.19 A·cm⁻²/Na₂Cr₂O₇)

Compound	Peak Binding Energy (e.V)	Area Ratio	FWHM fit param (eV)
Al_2O_3	74.16	1	1.34
Al_2O_3 -doublet	74.7	0.61	1.34
$Cr_2O_3-(O_2/Al)$	75.21	0.32	1.39

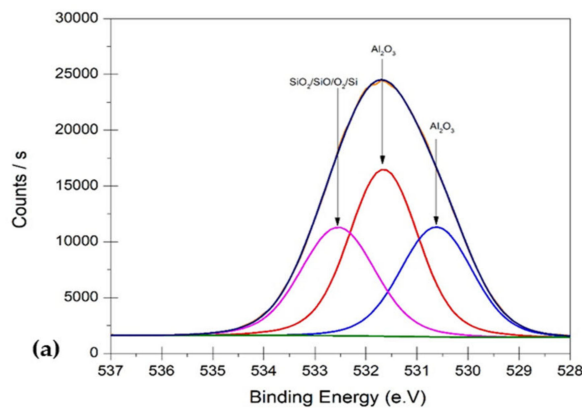
(c')

S4 (1.0 A·cm⁻²/Na₂Cr₂O₇)

Compound	Peak Binding Energy (e.V)	Area Ratio	FWHM fit param (eV)
$Al_2O_3/AlN/Al(OH)_3/AlN/Al_2S_3$	74.31	0.66	1.42
$Al_2O_3/AlN/Al(OH)_3/AlN/Al_2S_3$ -doublet	74.85	0.29	1.42
$(Al_2O_3/Al)/AlO(OH)$	76.34	1	2.45
$(Al_2O_3/Al)/AlO(OH)$ -doublet	76.88	0.56	2.45

(d')

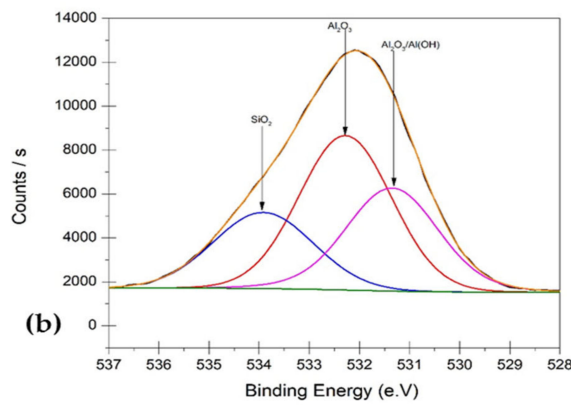
Figure 5. X-ray photoelectron spectra for Al-Li AA2055 alloy anodized: (a) Al 2p/S1, (b) Al 2p/S2, (c) Al 2p/S3, (d) Al 2p/S4. Parameters obtained from the peak binding energy and (FWHM) fitting (a') S1, (b') S2, (c') S3, (d') S4.



S1 (0.19 A·cm⁻²/H₂O)

Compound	Peak Binding Energy (e.V)	Area Ratio	FWHM fit param (eV)
Al ₂ O ₃	531.65	1	1.59
Al ₂ O ₃	530.62	0.68	1.66
SiO ₂ /SiO ₂ /(O ₂ /Si)	532.55	0.7	1.71

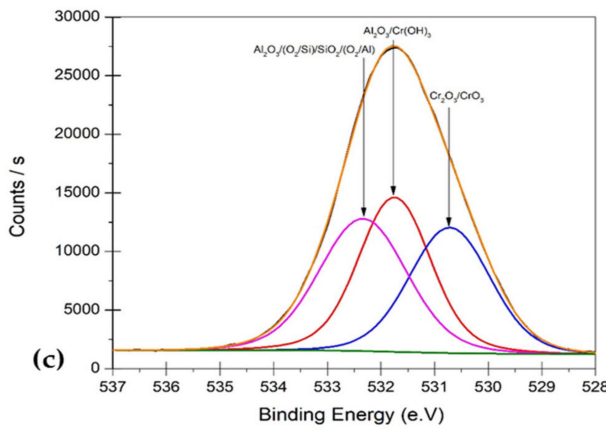
(a')



S2 (1.0 A·cm⁻²/H₂O)

Compound	Peak Binding Energy (e.V)	Area Ratio	FWHM fit param (eV)
Al ₂ O ₃	532.28	1	1.59
Al ₂ O ₃ /Al(OH) ₃	531.35	0.7	1.71
SiO ₂	533.92	0.68	1.66

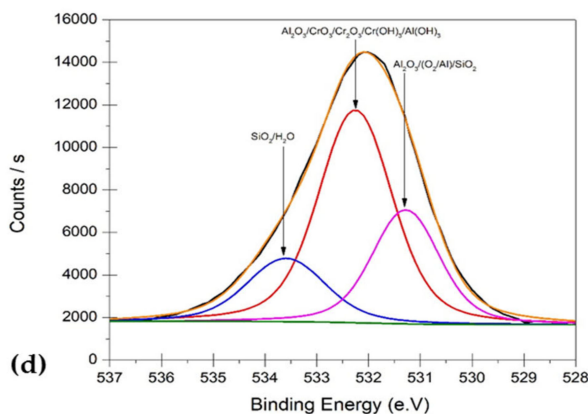
(b')



S3 (0.19 A·cm⁻²/Na₂Cr₂O₇)

Compound	Peak Binding Energy (e.V)	Area Ratio	FWHM fit param (eV)
Al ₂ O ₃ /Cr(OH) ₃	531.75	0.97	1.58
Cr ₂ O ₃ /CrO ₃	530.72	0.87	1.78
Al ₂ O ₃ /(O ₂ /Si)/SiO ₂ /(O ₂ /Al)	532.34	1	1.92

(c')



S4 (1.0 A·cm⁻²/Na₂Cr₂O₇)

Compound	Peak Binding Energy (e.V)	Area Ratio	FWHM fit param (eV)
Al ₂ O ₃ /(O ₂ /Al)/SiO ₂	531.28	0.49	1.53
SiO ₂ /H ₂ O	533.59	0.32	1.79
Al ₂ O ₃ /CrO ₃ /Cr ₂ O ₃ /Cr(OH) ₃ /Al(OH) ₃	532.26	1	1.68

(d')

Figure 6. X-ray photoelectron spectra for Al-Li AA2055 alloy anodized: (a) O 1s /S1, (b) O 1s/S2, (c) O 1s/S3, (d) O 1s/S4. Parameters obtained from the peak binding energy and (FWHM) fitting (a') S1, (b') S2, (c') S3, (d') S4.

The variations in the FWHM indicate changes in chemical state and physical influences. For example, if a peak broadening, corresponding to a possible change in the number of chemical bonds, that contributes to the shape of a peak, a change in sample conditions due to X-ray damage, or localized charge differences in the surface. Therefore, metals normally have lower FWHM values than metallic compounds [95]. There exist some substantial differences in the FWHM of the Al 2p peak, being narrower in the case of α -Al₂O₃ (FWHM of 1.35 eV), wider for hydroxides with FWHM values between 1.59 and 1.75 eV, and abnormally larger for γ -Al₂O₃ (FWHM of 2.46 eV) [96]. In this sense, we can see in Figure 5a' sample S1 that the FWHM values are close to the peak of the α -Al₂O₃ compound, presenting values between 1.25 and 1.38 eV, while for Figure 5b', they present FWHM values of 0.99 to 1.13 eV, which would indicate the presence of α -Al₂O₃ with a mixture of hydroxides, since there is an O 1s peak of 1.8 eV for sample S2. In the case of sample S3, Figure 5c', only FWHM values between 1.34 and 1.39 eV were observed, corresponding to α -Al₂O₃. Finally, for sample S4, Figure 5d', there is a combination between α -Al₂O₃ and γ -Al₂O₃ since the FWHM values are 1.42 and 2.45 eV in the four peaks present.

Anodizing current density influences the compounds that can be formed during the process, since, as can be seen in Figure 5a',c', the compounds formed with current densities of 0.19 A·cm⁻² correspond to α -Al₂O₃, as observed in the FWHM values of samples S1 and S3. In Figure 5b',d', which were the anodized samples with a current density of 1 A·cm⁻², there is the combination of α -Al₂O₃ compounds, hydroxides, and γ -Al₂O₃ since the FWHM for samples S2 and S4 present values of 0.99, 1.13, 1.8, and 2.45 eV. It is quite difficult to predictively calculate the O 1s interval between oxide and hydroxide, but it is interesting to note that, in aluminum compounds (Al–O), the bond is approximately the same length for oxide and hydroxide bonds, while in most other elements, the hydroxide bond is higher. One way to distinguish between oxide, hydroxide, and water compounds is through analysis in the O 1s region.

The O 1s peaks of aluminum oxides generally have values between 529 and 530 eV, which gives an interval of approximately 1 eV to distinguish between aluminum oxide and hydroxide compounds. Aluminum hydroxides have higher binding energy than oxides, which are in a binding energy range for the O 1s orbital between 0.5 and 0.75 eV. The usual values for the separation between oxide and hydroxide for most metals are in the interval of 1.5 to 2 eV, which makes it difficult to assign oxides and hydroxides in aluminum compounds [97]. In this work, O 1s peaks with binding energies from 530.62 to 532.34 eV were presented, which limits the possibility of distinguishing between oxides and hydroxides in this orbital. For aluminum compounds, the differences between oxides and hydroxides cannot be easily distinguished, since any of the oxides may have a peak in the O 1s orbital (529 to 530 eV). As can be seen in Figure 6a'–d', all binding energies fall outside the range proposed in the literature for the oxide region [97]. The FWHM of all the O 1s peaks is between 1.58 and 1.92 eV, giving a difference of 0.34 eV, which makes it difficult to assign aluminum oxide-hydroxide to the O 1s peaks.

4. Conclusions

- The results reveal that the EIS technique is a good tool for obtaining detailed information on the influence of sealing and the process on anodized aluminum.
- EIS results show that R₂ increase for the sample S₃ in presence of the Na₂Cr₂O₇ sealing solution has a higher charge transfer resistance when it has a less homogeneous and less compact layer of anodic oxide.
- The inductive loop present in Nyquist diagrams for all samples indicates species on the surface decreases, adsorption and electrodisolution of the oxide on the AA2055 alloys anodized surface.
- The SEM and EIS results indicated that the formation of a more compact and homogeneous anodic oxide layer is due to an increase in charge transfer resistance (R_{CT}), by preventing Cl⁻ ions ingress into the anodized layer.

- SEM characterization indicated that, in both current densities, the thickness is homogeneous for the oxide films formed on anodized AA2055 aluminum-lithium alloy. The surface micrographs indicated that samples have a heterogeneous surface with bumps, some bright precipitations, and cavity. This may be due to varying the current density and the sealing solutions during the growth of the Al₂O₃ layer in the H₂SO₄ bath.
- XPS characterization verified that the surface film of AA2055 alloy in this study consisted of a mixture of chemical compounds, such as Al₂O₃ and AlO(OH), respectively.

Author Contributions: Conceptualization, F.A.-C., P.O.S.-G. and C.G.-T.; methodology, J.C.-M., P.O.S.-G., L.D.L.-L., J.O.-C., L.G.S.V. and C.G.-T.; data curation, F.A.-C., L.G.S.V., E.M.-B., P.Z.-R., D.N.-M. and J.C.-M.; formal analysis, F.A.-C., P.O.S.-G. and C.G.-T.; writing—review and editing, F.A.-C., J.C.-M. and C.G.-T. All authors have read and agreed to the published version of the manuscript.

Funding: This research was funded by the Mexican National Council for Science and Technology (CONACYT) of the projects A1-S-8882 and the Universidad Autónoma de Nuevo León (UANL).

Institutional Review Board Statement: Not applicable.

Informed Consent Statement: Not applicable.

Data Availability Statement: The data presented in this study are available on request from the corresponding author.

Acknowledgments: The authors would like to thank the Mexican National Council for Science and Technology (CONACYT) for the support provided for the development of the projects A1-S-8882, the UANL-CA-316 working group and Universidad Autónoma de Nuevo León (UANL) for the facilities given to develop this investigation.

Conflicts of Interest: The authors declare no conflict of interest.

References

1. Saffari, H.; Sohrabi, B.; Noori, M.R.; Bahrami, H.R.T. Optimal condition for fabricating superhydrophobic aluminum surfaces with controlled anodizing processes. *Appl. Surf. Sci.* **2018**, *435*, 1322–1328. [\[CrossRef\]](#)
2. Jiang, B.; Yi, D.; Yi, X.; Zheng, F.; Wang, H.; Wang, B.; Hu, Z. Effect of trace amounts of added Sc on microstructure and mechanical properties of 2055 aluminum alloy. *Mater. Charact.* **2018**, *141*, 248–259. [\[CrossRef\]](#)
3. Keller, F.; Hunter, M.S.; Robinson, D.L. Structural features of oxide coatings on aluminum. *J. Electrochem. Soc.* **1953**, *100*, 411–419. [\[CrossRef\]](#)
4. Jaimes-Ramírez, R.; Covelo, A.; Rodil, S.E.; Corona-Lira, P.; Ramírez-Reivich, A.C.; Hernández, M. Development and characterization of hydrophobic anodized aluminum layer to act as a long-lasting protective film in corrosion. *Surf. Interface Anal.* **2018**, *50*, 1030–1035. [\[CrossRef\]](#)
5. Etienne, M.; Rocca, E.; Chahboun, N.; Veys-Renaux, D. Local evolution of pH with time determined by shear force-based scanning electrochemical microscopy: Surface reactivity of anodized aluminium. *Electroanalysis* **2016**, *28*, 2466–2471. [\[CrossRef\]](#)
6. Zhang, F.; Örnek, C.; Nilsson, J.-O.; Pan, J. Anodisation of aluminium alloy AA7075-influence of intermetallic particles on anodic oxide growth. *Corros. Sci.* **2020**, *164*, 108319. [\[CrossRef\]](#)
7. Ma, Y.; Chen, X.; Zhou, X.; Yi, Y.; Liao, Y.; Huang, W. Microstructural origin of localized corrosion in anodized AA2099-T8 aluminium-lithium alloy. *Surf. Interface Anal.* **2016**, *48*, 739–744. [\[CrossRef\]](#)
8. Mouritz, P.A. *Introduction to Aerospace Materials*; Woodhead Publishing: Cambridge, UK, 2012.
9. Zhou, X.R.; Meng, X.M.; Huang, W.J.; Yi, L.; Chen, X.L.; Yi, Y.N.; Thompson, G.E. Influence of thermomechanical treatments on localized corrosion susceptibility and propagation mechanism of AA2099 Al–Li alloy. *Trans. Nonferrous Met. Soc.* **2016**, *26*, 1472–1481. [\[CrossRef\]](#)
10. Gumbmann, E.; Lefebvre, W.; De Geuser, F.; Sigli, C.; Deschamps, A. The effect of minor solute additions on the precipitation path of an Al Cu Li alloy. *Acta Mater.* **2016**, *115*, 104–114. [\[CrossRef\]](#)
11. Gumbmann, E.; De Geuser, F.; Deschamps, A.; Lefebvre, W.; Robaut, F.; Sigli, C. A combinatorial approach for studying the effect of Mg concentration on precipitation in an Al–Cu–Li alloy. *Scr. Mater.* **2016**, *110*, 44–47. [\[CrossRef\]](#)
12. Ma, Y.; Zhou, X.; Huang, W.; Liao, Y.; Chen, X.; Zhang, X.; Thompson, G.E. Crystallographic defects induced localised corrosion in AA2099-T8 aluminium alloy. *Corros. Eng. Sci. Technol.* **2015**, *50*, 420–424. [\[CrossRef\]](#)
13. Deschamps, A.; Garcia, M.; Chevy, J.; Davo, B.; De Geuser, F. Influence of Mg and Li content on the microstructure evolution of Al Cu Li alloys during long-term ageing. *Acta Mater.* **2017**, *122*, 32–46. [\[CrossRef\]](#)
14. Deng, Y.; Bai, J.; Wu, X.; Huang, G.; Cao, L.; Huang, L. Investigation on formation mechanism of T1 precipitate in an Al-Cu-Li alloy. *J. Alloys Compd.* **2017**, *723*, 661–666. [\[CrossRef\]](#)

15. Deschamps, A.; Decreus, B.; De Geuser, F.; Dorin, T.; Weyland, M. The influence of precipitation on plastic deformation of Al–Cu–Li alloys. *Acta Mater.* **2013**, *61*, 4010–4021. [[CrossRef](#)]
16. Eswara, P.N.; Gokhale, A.A.; Wanhill, H.J.R. *Aluminium-Lithium: Processing, Properties and Applications*; Butterworth-Heinemann; Elsevier Inc.: Waltham, MA, USA, 2014. [[CrossRef](#)]
17. Ma, Y.; Zhou, X.; Thompson, G.E.; Curioni, M.; Zhong, X.; Koroleva, E.; Fowles, M. Discontinuities in the porous anodic film formed on AA2099-T8 aluminium alloy. *Corros. Sci.* **2011**, *53*, 4141. [[CrossRef](#)]
18. Vignoli Machado, T.; Atz Dick, P.; Knörschild, G.H.; Dick, L.F.P. The effect of different carboxylic acids on the sulfuric acid anodizing of AA2024. *Surf. Coat. Technol.* **2020**, *383*, 125283. [[CrossRef](#)]
19. Runge, J.M. *The Metallurgy of Anodizing Aluminum*; Springer: Chicago, IL, USA, 2018. [[CrossRef](#)]
20. Varshney, D.; Kumar, K. Application and use of different aluminium alloys with respect to workability, strength and welding parameter optimization. *Ain Shams Eng. J.* **2021**, *12*, 1143–1152. [[CrossRef](#)]
21. Ambor, M.; Nový, F.; Bokůvka, O.; Trško, L. The natural aging behavior of the AA 2055 Al-Cu-Li alloy. *Transp. Res. Procedia* **2019**, *40*, 42–45. [[CrossRef](#)]
22. Mopon, M.L., Jr.; Garcia, J.S.; Manguerra, D.M.; Narisma, C.J.C. Corrosion behavior of AA 1100 anodized in gallic-sulfuric acid solution. *Coatings* **2021**, *11*, 405. [[CrossRef](#)]
23. Raj, V.; Mumjitha, M. Comparative study of formation and corrosion performance of porous alumina and ceramic nanorods formed in different electrolytes by anodization. *Mater. Sci. Eng. B Solid-State Mater. Adv. Technol.* **2014**, *179*, 25–35. [[CrossRef](#)]
24. Martínez-Viademonte, M.P.; Abrahami, S.T.; Hack, T.; Burchardt, M.; Terryn, H. A review on anodizing of aerospace aluminum alloys for corrosion protection. *Coatings* **2020**, *10*, 1106. [[CrossRef](#)]
25. Cabral-Miramontes, J.; Gaona-Tiburcio, C.; Estupinán-López, F.; Lara-Banda, M.; Zambrano-Robledo, P.; Nieves-Mendoza, D.; Maldonado-Bandala, E.; Chacón-Nava, J.; Almeraya-Calderón, F. Corrosion resistance of hard coat anodized AA 6061 in citric-sulfuric solutions. *Coatings* **2020**, *10*, 601. [[CrossRef](#)]
26. Cabral-Miramontes, J.A.; Gaona-Tiburcio, C.; Almeraya-Calderón, F.; Estupiñan-Lopez, H.F.; Pedraza-Basulto, G.; Poblano-Salas, C. Parameter studies on high-velocity oxy-fuel spraying of CoNiCrAlY coatings used in the aeronautical industry. *Int. J. Corros.* **2014**, *2014*, 1–8. [[CrossRef](#)]
27. Zuo, Y.; Zhao, P.-H.; Zhao, J.-M. The influences of sealing methods on corrosion behavior of anodized aluminum alloys in NaCl solutions. *Surf. Coat. Technol.* **2003**, *166*, 237–242. [[CrossRef](#)]
28. Ko, C.-L.; Kuo, Y.-L.; Chen, S.-H.; Chen, S.-Y.; Guo, J.-Y.; Wang, Y.-J. Formation of aluminum composite passive film on magnesium alloy by integrating sputtering and anodic aluminum oxidation processes. *Thin Solid Films* **2020**, *709*, 138151. [[CrossRef](#)]
29. Gianni, L.; Cavallini, M.; Natali, S.; Adriaens, S. Wet and dry accelerated aging tests in a spray chamber to understand the effects of acid rain frequencies on bronze corrosion. *Int. J. Electrochem. Sci.* **2013**, *8*, 1822–1838.
30. ASTM E3-95. *Standard Practice for Preparation of Metallographic Specimens*; ASTM International: West Conshohocken, PA, USA, 1995.
31. Samaniego-Gámez, P.; Almeraya-Calderón, F.; Martin, U.; Ress, J.; Gaona-Tiburcio, C.; Silva-Vidaurre, L.; Cabral-Miramontes, J.; Bastidas, J.M.; Chacón-Nava, J.G.; Bastidas, D.M. Efecto del tratamiento de sellado en el comportamiento frente a corrosión de la aleación anodizada de aluminio-litio AA2099. *Rev. Met.* **2020**, *56*, e180. [[CrossRef](#)]
32. ASTM G106-15. *Standard Practice for Verification of Algorithm and Equipment for Electrochemical Impedance Measurements*; ASTM International: West Conshohocken, PA, USA, 2010.
33. Macdonald, D.D. Review of mechanistic analysis by electrochemical impedance spectroscopy. *Electrochim. Acta* **1990**, *35*, 1509–1525. [[CrossRef](#)]
34. Yang, Y.; Cheng, J.; Liu, S.; Wang, H.; Dong, P. Effect of NaAlO₂ sealing on corrosion resistance of 2024 aluminum alloy anodized film. *Mater. Corros.* **2019**, *70*, 120–127. [[CrossRef](#)]
35. Cabral-Miramontes, J.; Bastidas, M.D.; Baltazar, M.A.; Zambrano-Robledo, P.; Bastidas, J.M.; Almeraya-Calderón, F.; Gaona-Tiburcio, C. Corrosion behavior of Zn-TiO₂ and Zn-ZnO electrodeposited coatings in 3.5% NaCl solution. *Int. J. Electrochem. Sci.* **2019**, *14*, 4226–4239. [[CrossRef](#)]
36. Gaona-Tiburcio, C.; Montoya-Rangel, M.; Cabral-Miramontes, J.A.; Estupiñan-López, F.; Zambrano-Robledo, P.; Orozco Cruz, R.; Chacón-Nava, J.G.; Baltazar-Zamora, M.A.; Almeraya-Calderón, F. Corrosion resistance of multilayer coatings deposited by PVD on Inconel 718 using electrochemical impedance spectroscopy technique. *Coatings* **2020**, *10*, 521. [[CrossRef](#)]
37. Herrera-Hernandez, H.; Vargas-García, J.R.; Hallen-López, J.M.; Mansfeld, F. Evaluation of different sealing methods for anodized aluminum-silicon carbide (Al/SiC) composites using EIS and SEM techniques. *Mater. Corros.* **2007**, *58*, 825–832. [[CrossRef](#)]
38. Ma, T.; Wua, H.; Zhou, X.; Lic, K.; Liaod, Y.; Lianga, Z.; Liua, L. Corrosion behavior of anodized Al-Cu-Li alloy: The role of intermetallic particle-introduced film defects. *Corros. Sci.* **2019**, *58*, 108110. [[CrossRef](#)]
39. Wu, H.; Ma, Y.; Huang, W.; Zhou, X.; Li, K.; Liao, Y.; Wang, Z.; Liang, Z.; Liu, L. Effect of iron-containing intermetallic particles on film structure and corrosion resistance of anodized AA2099 alloy. *J. Electrochem. Soc.* **2018**, *165*, C573–C581. [[CrossRef](#)]
40. Schneider, M.; Kremmer, K. Corrosion behavior of anodized AA-6060 depending on the anodizing bath aging. *Mater. Corros.* **2019**, *70*, 2041–2051. [[CrossRef](#)]
41. Gao, Z.; Cao, J.; Chen, Y.; Muzammal, H.M.; Wang, W. Effect of Cu preferential orientation on the microstructure and property of anodized Cu₂O film. *Eur. J. Inorg. Chem.* **2020**, *2020*, 261–268. [[CrossRef](#)]
42. Zeng, D.; Liu, Z.; Bai, S.; Wang, J. Influence of sealing treatment on the corrosion resistance of PEO coated Al-Zn-Mg-Cu alloy in various environments. *Coatings* **2019**, *9*, 867. [[CrossRef](#)]

43. Hua, L.; Liu, J.; Li, S.; Yu, M. Effect of adipic acid on deis characteristics during the aluminium anodizing process in sulfuric acid bath. *Int. J. Electrochem. Sci.* **2015**, *10*, 2194–2205.
44. Brett, C.M.A. The application of electrochemical impedance techniques to aluminium corrosion in acidic chloride Solution. *J. App. Electrochem.* **1990**, *20*, 1000–1003. [[CrossRef](#)]
45. Bastidas, D.M. Interpretation of impedance data for porous electrodes and diffusion processes. *Corrosion* **2007**, *63*, 515–521. [[CrossRef](#)]
46. Jirón-Lazos, U.; Corvo, F.; De la Rosa-García, S.; García-Ochoa, E.; Bastidas, D. Localized corrosion of aluminum alloy 6061 in the presence of *Asper gillus niger*. *Int. Biodeter. Boidegr.* **2018**, *133*, 17–25. [[CrossRef](#)]
47. Jinlong, L.; Tongxiang, L.; Chen, W.; Ting, G. The passive film characteristics of several plastic deformation 2099 Al–Li alloy. *J. Alloys Compd.* **2016**, *662*, 143–149. [[CrossRef](#)]
48. Pivac, I.; Barbir, F. Inductive phenomena at low frequencies in impedance spectra of proton exchange membrane fuel cells—A review. *J. Power Sources* **2016**, *326*, 112–119. [[CrossRef](#)]
49. Alexe-Ionescu, A.L.; Barbero, G.; Evangelista, L.R.; Lenzi, E.K. Current–voltage characteristics and impedance spectroscopy: Surface conduction and adsorption–desorption effects in electrolytic cells. *J. Phys. Chem. C* **2020**, *124*, 3150–3158. [[CrossRef](#)]
50. Djellab, M.; Bentrach, H.; Chala, A.; Taoui, H. Synergistic effect of halide ions and gum arabic for the corrosion inhibition of API5L X70 pipeline steel in H₂SO₄. *Mater. Corros.* **2019**, *70*, 149–160. [[CrossRef](#)]
51. Bastidas, J.M.; Polo, J.; Torres, C.; Cano, E. A study on the stability of AISI 316L stainless steel pitting corrosion through its transfer function. *Corros. Sci.* **2001**, *43*, 269–281. [[CrossRef](#)]
52. Klotz, D. Negative capacitance or inductive loop?—A general assessment of a common low frequency impedance feature. *Electrochem. Commun.* **2019**, *98*, 58–62. [[CrossRef](#)]
53. Usman, B.J.; Scenini, F.; Curioni, M. Corrosion testing of anodized aerospace alloys: Comparison between immersion and salt spray testing using electrochemical impedance spectroscopy. *J. Electrochem. Soc.* **2020**, *167*, 041505. [[CrossRef](#)]
54. Huang, Y.; Shih, H.; Huang, H.; Daugherty, J.; Wu, S.; Ramanathan, S.; Chang, C.; Mansfeld, F. Evaluation of the corrosion resistance of anodized aluminum 6061 using electrochemical impedance spectroscopy (EIS). *Corros. Sci.* **2008**, *50*, 3569–3575. [[CrossRef](#)]
55. Zapata-Loría, A.D.; Pech-Canul, M.A. Corrosion inhibition of aluminum in 0.1 M HCL solution by glutamic acid. *Chem. Eng. Commun.* **2014**, *201*, 855–869. [[CrossRef](#)]
56. Suay, J.; Giménez, E.; Rodríguez, T.; Habbib, K.; Saura, J. Characterization of anodized and sealed aluminium by EIS. *Corros. Sci.* **2003**, *45*, 611–624. [[CrossRef](#)]
57. Wang, S.; Peng, H.; Shao, Z.; Zhao, Q.; Du, N. Sealing of anodized aluminum with phytic acid solution. *Surf. Coat. Technol.* **2015**, *286*, 155–164. [[CrossRef](#)]
58. Saeedikhani, M.; Javid, M.; Yazdani, A. Anodizing of 2024-T3 aluminum alloy in sulfuric-boric-phosphoric acids and its corrosion behavior. *Trans. Nonferrous Met. Soc. China* **2013**, *23*, 2551–2559. [[CrossRef](#)]
59. Hsu, C.H.; Mansfeld, F. Technical note: Concerning the conversion of the constant phase element parameter Y₀ into a capacitance. *Corrosion* **2001**, *57*, 747–748. [[CrossRef](#)]
60. Scully, J.R.; Silverman, D.C.; Kendig, M.W. *Electrochemical Impedance: Analysis and Interpretation STP 1188*; ASTM International: Philadelphia, PA, USA, 1993. [[CrossRef](#)]
61. Pérez, N. *Electrochemistry and Corrosion Science*; Springer: New York, NY, USA, 2004.
62. Hirschorn, B.; Orazem, M.E.; Tribollet, B.; Vivier, V.; Frateur, I.; Musiani, M. Determination of effective capacitance and film thickness from constant-phase-element parameters. *Electrochim. Acta* **2010**, *55*, 6218–6227. [[CrossRef](#)]
63. Evertsson, J.; Bertram, F.; Rullik, L.; Harlow, G.; Lundgren, E. Anodization of Al (100), Al (111) and Al Alloy 6063 studied in situ with X-ray reflectivity and electrochemical impedance spectroscopy. *J. Electroanal. Chem.* **2017**, *799*, 556–562. [[CrossRef](#)]
64. Cabral-Miramontes, J.A.; Barceinas-Sánchez, J.D.O.; Poblano-Salas, C.A.; Pedraza-Basulto, G.K.; Nieves-Mendoza, D.; Zambrano-Robledo, P.C.; Almeraya-Calderón, F.; Chacón-Nava, J.G. Corrosion behavior of AISI 409Nb stainless steel manufactured by powder metallurgy exposed in H₂SO₄ and NaCl solutions. *Int. J. Electrochem. Sci.* **2013**, *8*, 564–577.
65. Ayagou, M.D.D.; Tran, T.T.M.; Tribollet, B.; Kittel, J.; Sutter, E.; Ferrando, N.; Mendibide, C.; Duret-Thual, C. Electrochemical impedance spectroscopy of iron corrosion in H₂S solutions. *Electrochim. Acta* **2018**, *282*, 775–783. [[CrossRef](#)]
66. Núñez-Jaquez, R.E.; Buelna-Rodríguez, J.E.; Barrios-Durstewitz, C.P.; Gaona-Tiburcio, C.; Almeraya-Calderón, F. Corrosion of modified concrete with sugar cane bagasse ash. *Int. J. Corros.* **2012**, *2012*, 1–5. [[CrossRef](#)]
67. Zhao, X.-H.; Zuo, Y.; Zhao, J.-M.; Xiong, J.-P.; Tang, Y.-M. A study on the self-sealing process of anodic films on aluminum by EIS. *Surf. Coat. Technol.* **2006**, *200*, 6846–6853. [[CrossRef](#)]
68. Khadiri, M.; Elyagoubi, M.; Idouhli, R.; Koumya, Y.; Zakir, O.; Benzakour, J.; Benyaich, A.; Abouelfida, A.; Outzourhit, A. Electrochemical study of anodized titanium in phosphoric acid. *Adv. Mater. Sci. Eng.* **2020**, *2020*, 1–11. [[CrossRef](#)]
69. Ono, S.; Asoh, H. Mechanism of hot water sealing of anodic films formed on aluminum. *Corros. Sci.* **2021**, *181*, 109221. [[CrossRef](#)]
70. Martínez-Villafañe, A.; Chacon-Nava, J.; Gaona-Tiburcio, C.; Almeraya-Calderon, F.; Domínguez-Patiño, G.; Gonzalez-Rodríguez, J. Oxidation performance of a Fe–13Cr alloy with additions of rare earth elements. *Mater. Sci. Eng. A* **2003**, *363*, 15–19. [[CrossRef](#)]
71. Boukamp, B.A. Interpretation of an ‘inductive loop’ in the impedance of an oxygen ion conducting electrolyte/metal electrode system. *Solid State Ion.* **2001**, *143*, 47–55. [[CrossRef](#)]

72. Corral, H.R.; Arredondo, R.S.P.; Neri, F.M.; Gómez, S.J.M.; Almeraya, C.F.; Castorena, G.J.H.; Almaral, S.J. Sulfate attack and reinforcement corrosion in concrete with recycled concrete aggregates and supplementary cementing materials. *Int. J. Electrochem. Sci.* **2011**, *6*, 613–621.
73. Ofoegbu, S.U.; Fernandes, F.A.; Pereira, A.B. The sealing step in aluminum anodizing: A focus on sustainable strategies for enhancing both energy efficiency and corrosion resistance. *Coatings* **2020**, *10*, 226. [[CrossRef](#)]
74. Miramontes, J.A.C.; Sánchez, J.D.O.B.; Calderón, F.A.; Villafañe, A.M.; Nava, J.G.C. Effect of boron additions on sintering and densification of a ferritic stainless steel. *J. Mater. Eng. Perform.* **2010**, *19*, 880–884. [[CrossRef](#)]
75. Macdonald, D.D.; Sikora, E.; Engelhardt, G. Characterizing electrochemical systems in the frequency domain. *Electrochim. Acta* **1998**, *43*, 87–107. [[CrossRef](#)]
76. Cao, C.-N. On the impedance plane displays for irreversible electrode reactions based on the stability conditions of the steady-state—II. Two state variables besides electrode potential. *Electrochim. Acta* **1990**, *35*, 837–844. [[CrossRef](#)]
77. Clerc, C.; Landolt, D. AC impedance study of anodic films on nickel in LiCl. *Electrochim. Acta* **1988**, *33*, 859–871. [[CrossRef](#)]
78. Elkin, V.V.; Marshakov, A.I.; Rybkina, A.A.; Maleeva, M. Interpretation of the impedance comprising negative capacitance and constant phase elements on iron electrode in weakly acidic media. *Russ. J. Electrochem.* **2011**, *47*, 136–146. [[CrossRef](#)]
79. Strohmeier, B.R. An ESCA method for determining the oxide thickness on aluminum alloys. *Surf. Interface Anal.* **1990**, *15*, 51–56. [[CrossRef](#)]
80. Pérez, O.E.L.; Sánchez, M.D.; Teijelo, M.L. Characterization of growth of anodic antimony oxide films by ellipsometry and XPS. *J. Electroanal. Chem.* **2010**, *645*, 143–148. [[CrossRef](#)]
81. Alexander, M.R.; Thompson, G.E.; Beamson, G. Characterization of the oxide/hydroxide surface of aluminium using X-ray photoelectron spectroscopy: A procedure for curve fitting the O 1s core level. *Surf. Interface Anal.* **2000**, *29*, 468–477. [[CrossRef](#)]
82. Feliu, S.; Bartolomé, M.J.; González, J.A.; Feliu, S. XPS characterization of porous and sealed anodic films on aluminum alloys. *J. Electrochem. Soc.* **2007**, *154*, C241–C248. [[CrossRef](#)]
83. Caicedo-Martinez, C.E.; Koroleva, E.; Skeldon, P.; Thompson, G.E.; Hoellrigl, G.; Bailey, P.; Noakes, T.C.Q.; Habazaki, H.; Shimizu, K. Behavior of impurity and minor alloying elements during surface treatments of aluminum. *J. Electrochem. Soc.* **2002**, *149*, B139–B145. [[CrossRef](#)]
84. Paez, A.M.; Bustos, O.; Thompson, E.G.; Skeldon, P.; Shimizu, K.; Wood, C.G. Porous anodic film formation on an Al-3.5 wt.% Cu Alloy. *J. Electrochem. Soc.* **2000**, *147*, 1015. [[CrossRef](#)]
85. Romios, M.; Tiraschi, R.; Parrish, C.; Babel, H.W.; Ogren, J.R.; Es-Said, O.S. Design of multistep aging treatments of 2099 (C458) Al-Li Alloy. *J. Mater. Eng. Perform.* **2005**, *14*, 641–646. [[CrossRef](#)]
86. Abrahami, S.; Hauffman, T.; De Kok, J.M.; Mol, A.; Terry, H. XPS analysis of the surface chemistry and interfacial bonding of barrier-type Cr (VI)-free anodic oxides. *J. Phys. Chem. C* **2015**, *119*, 19967–19975. [[CrossRef](#)]
87. Skeldon, P.; Wang, H.; Thompson, G. Formation and characterization of self-lubricating MoS₂ precursor films on anodized aluminium. *Wear* **1997**, *206*, 187–196. [[CrossRef](#)]
88. Khan, M.F.; Kumar, A.M.; Ul-Hamid, A.; Al-Hems, L.M. Achieving non-adsorptive anodized film on Al-2024 alloy: Surface and electrochemical corrosion investigation. *Surf. Interfaces* **2019**, *15*, 78–88. [[CrossRef](#)]
89. Ryu, S.-K.; Park, B.-J.; Park, S.-J. XPS analysis of carbon fiber surfaces—Anodized and interfacial effects in fiber-epoxy composites. *J. Colloid Interface Sci.* **1999**, *215*, 167–169. [[CrossRef](#)]
90. Duong, L.V.; Wood, B.J.; Klopogge, J.T. XPS study of basic aluminum sulphate and basic aluminium nitrate. *Mater. Lett.* **2005**, *59*, 1932–1936. [[CrossRef](#)]
91. Zähr, J.; Oswald, S.; Türpe, M.; Ullrich, H.; Füssel, U. Characterisation of oxide and hydroxide layers on technical aluminum materials using XPS. *Vacuum* **2012**, *86*, 1216–1219. [[CrossRef](#)]
92. Martínez-Villafañe, A.; Almeraya-Calderón, M.; Gaona-Tiburcio, C.; Gonzalez-Rodriguez, J.; Porcayo-Calderon, J. High-temperature degradation and protection of ferritic and austenitic steels in steam generators. *J. Mater. Eng. Perform.* **1998**, *7*, 108–113. [[CrossRef](#)]
93. Zhang, Z.; Zhang, Y.; Guo, Y.; Chen, X.; Chen, L. Impurity element analysis of aluminum hydride using PIXE, XPS and elemental analyzer technique. *Nucl. Instrum. Methods. Phys. Res. B Beam Interact. Mater. At.* **2021**, *488*, 1–4. [[CrossRef](#)]
94. Ramirez-Arteaga, A.M.; Gonzalez-Rodriguez, J.G.; Campillo, B.; Gaona-Tiburcio, C.; Dominguez-Patiño, G.; Leduc Lezama, L.; Chacon-Nava, J.G.; Neri-Flores, M.A.; Martinez-Villafañe, A. An electrochemical study of the corrosion behavior of a dual phase steel in 0.5 m H₂SO₄. *Int. J. Electrochem. Sci.* **2010**, *5*, 1786–1798.
95. Vac, J. Practical guide for curve fitting in X-ray photoelectron spectroscopy. *Sci. Technol.* **2020**, *38*, 061203. [[CrossRef](#)]
96. Sherwood, P.M.A. Introduction to studies of aluminum and its compounds by XPS. *Surf. Sci. Spectra* **1998**, *5*, 1–3. [[CrossRef](#)]
97. Paparazzo, E. XPS and auger spectroscopy studies on mixtures of the oxides SiO₂, Al₂O₃, Fe₂O₃ and Cr₂O₃. *J. Electron Spectrosc. Relat. Phenom.* **1987**, *43*, 97–112. [[CrossRef](#)]

Reproduced with permission of copyright owner. Further reproduction prohibited without permission.